X-ray restrained extremely localized molecular orbitals for the embedding of quantum mechanical calculations

Giovanni Macetti, Piero Macchi, Alessandro Genoni

STRUCTURAL SCIENCE
CRYSTAL ENGINEERING
MATERIALS

ISSN: 2052-5206
journals.iucr.org/b

X-ray restrained extremely localized molecular orbitals for the embedding of quantum mechanical calculations

Giovanni Macetti, Piero Macchi and Alessandro Genoni

Acta Cryst. (2021). B**77**, 695–705

STRUCTURAL SCIENCE
CRYSTAL ENGINEERING
MATERIALS

ISSN 2052-5206

X-ray restrained extremely localized molecular orbitals for the embedding of quantum mechanical calculations

Giovanni Macetti,[a] Piero Macchi[b] and Alessandro Genoni[a]*

[a]Université de Lorraine and CNRS, Laboratoire de Physique et Chimie Théoriques, 1 Boulevard Arago, Metz, F-57078, France, and [b]Department of Chemistry, Materials and Chemical Engineering, Politecnico di Milano, via Mancinelli 7, Milano, I-20131, Italy. *Correspondence e-mail: alessandro.genoni@univ-lorraine.fr

Received 30 June 2021
Accepted 15 August 2021

Edited by J.-M. Gillet, CentraleSupelec, France

Keywords: X-ray restrained wavefunction (XRW); extremely localized molecular orbitals (ELMOs); quantum embedding; quantum crystallography; QM/ELMO method.

Supporting information: this article has supporting information at journals.iucr.org/b

The X-ray restrained wavefunction (XRW) method is a quantum crystallographic technique that allows the calculation of molecular wavefunctions adapted to minimize the difference between computed and reference structure factor amplitudes. The latter result from experimental measurements on crystals or from advanced theoretical calculations with periodic boundary conditions, and are used as external restraints in a traditional least-squares structural refinement. Detailed investigations have shown that the technique is able to reliably capture the effects of the crystal field on the molecular electron density. In a recent application, electron distributions obtained from preliminary X-ray restrained wavefunction calculations have been employed in the framework of frozen density embedding theory to embed excited state computations of well defined subsystems. Inspired by these results, it was decided to test, for the first time, the X-ray restrained extremely localized molecular orbitals (XR-ELMOs) along with the recently developed quantum mechanics/extremely localized molecular orbital multiscale embedding approach. By exploiting XR-ELMOs obtained through XRW calculations that used structure factor amplitudes resulting from periodic *ab initio* computations, excited state calculations of acrylamide in an environment mimicking the one of the crystal structure were performed. In all these computations, the QM region coincides with the crystal asymmetric unit and the ELMO subsystem consisted of two other acrylamide molecules involved in direct hydrogen bonds with the reference unit. The shifts of the excitation energies with respect to the corresponding gas-phase values were evaluated as a function of different parameters on which the computations with XR-ELMOs depend. For instance, the dependence on the resolution of the sets of structure factors that were used to determine the embedding XR-ELMOs were assessed in particular. The results have shown that the use of XR-ELMOs slightly (but not negligibly) improves the description of excited states compared to the gas-phase ELMOs. Once again, these results demonstrate the efficiency of the XRW approach in incorporating environment effects into the calculated molecular orbitals and, hence, into the corresponding electron densities.

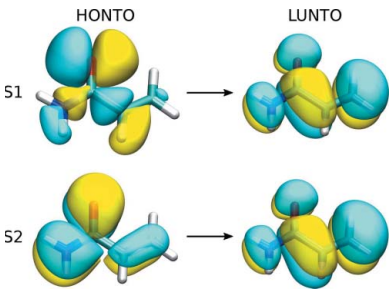

1. Introduction

The X-ray restrained wavefunction (XRW) approach, originally introduced by Jayatilaka (1998), is arguably one of the cornerstones of modern quantum crystallography (Genoni *et al.*, 2018; Grabowsky *et al.*, 2017; Massa & Matta, 2018; Genoni & Macchi, 2020; Grabowsky *et al.*, 2020; Macchi, 2020). The technique consists in determining wavefunctions that not only variationally minimize the energy of the system, but also reproduce a set of collected structure factor amplitudes within the experimental uncertainty. Initially proposed in the

framework of the restricted Hartree–Fock case (Jayatilaka, 1998; Jayatilaka & Grimwood, 2001; Grimwood & Jayatilaka, 2001; Bytheway *et al.*, 2002; Bytheway, Grimwood, Figgis *et al.*, 2002; Grimwood *et al.*, 2003), the strategy gradually evolved over the years and was combined with different quantum chemical methods. Apart from the straightforward extensions to the unrestricted Hartree–Fock formalism (Hudák *et al.*, 2010) and to density functional theory (DFT) (Jayatilaka, 2012), the technique was later coupled with the Douglas–Kroll–Hess (Hudák *et al.*, 2010) and infinite-order two-component (Bučinský *et al.*, 2016) relativistic approaches, with multi-determinant valence bond-like strategies (Genoni, 2017; Casati *et al.*, 2017; Genoni, Franchini *et al.*, 2018; Genoni, Macetti, Franchini *et al.*, 2019), and, more importantly for this work, with the Stoll method (Stoll *et al.*, 1980; Fornili *et al.*, 2003) for the determination of extremely localized molecular orbitals (ELMOs; see more details below and in *Theory*) (Genoni, 2013*a*,*b*; Dos Santos *et al.*, 2014; Genoni & Meyer, 2017).

In addition to this methodological development, the Jayatilaka strategy was also successfully exploited to gain insights into chemical bonding. The first attempt was certainly the one carried out by Jayatilaka & Grimwood (2004). They determined electron localization functions (ELFs) associated with XRWs and analyzed the differences with respect to corresponding gas-phase results to highlight the effects due to the crystal environment. Along this line, Grabowsky and coworkers also proposed a series of XRW-based chemical bonding studies, in which they computed localizability indicator domains to investigate the effects of the crystal field and of the substituents on a series of acceptor-substituted epoxide derivatives (Grabowsky *et al.*, 2010) and to explain the different reactivities of α,β-unsaturated carbonyl and hydrazone compounds (Grabowsky *et al.*, 2011). Afterwards, to perform complementary bonding analyses, Grabowsky and collaborators also simultaneously combined the XRW technique with different chemical bonding descriptors to tackle specific chemical problems from different angles. For instance, this approach was used for the investigation of hypervalency in sulfur dioxide (Grabowsky *et al.*, 2012), and in phosphate, sulfate and perchlorate anions (Fugel *et al.*, 2019). Similar strategies were also exploited by Thomas *et al.*, who applied bonding analyses based on the XRW method to shed light on the main features of chalcogen bonds (Thomas *et al.*, 2015; Grabowsky *et al.*, 2020).

X-ray restrained wavefunctions have been also employed in solid-state and materials science simulations. Pioneering works are those by Spackman, Jayatilaka and collaborators with the main goal of obtaining experimental (hyper)polarizabilities and refractive indices for some molecular crystals (Whitten *et al.*, 2006; Jayatilaka *et al.*, 2009). They proved that a wavefunction is fundamental to at least obtain approximate values of these properties, while the (experimental) electron density alone would not be sufficient. Their investigation also showed for the first time the intrinsic XRW capability of capturing crystal field effects using experimental structure factor amplitudes as restraints. This was later confirmed by Hickstein *et al.* (Hickstein *et al.*, 2013; Cole & Hickstein, 2013) for non-linear optical properties of different molecular materials, and, above all, by Ernst *et al.* (2020), who recently conducted a dedicated study to fully explore this aspect. In fact, in analogy with the conclusions of a previous investigation on the capability of the XRW method in capturing electron correlation effects (Genoni, Dos Santos *et al.*, 2017), Ernst *et al.* proved that the XRW approach is indeed able to incorporate the effects of the crystal field environment into the determined electron densities and molecular orbitals, although this is generally more evident when only medium and low-angle reflections are used as external restraints. Grabowsky *et al.* (2020) and collaborators drew similar conclusions in a preliminary study on the same topic.

A remark is necessary here. By coupling a molecular wavefunction calculation with a set of observables measured or calculated for an ideal crystal, the Jayatilaka technique inherently introduces two biases. In fact, so far (*a*) the Hamiltonian and the wavefunction are exclusively molecular, with the overall crystal wavefunction being the product of wavefunctions corresponding to non-interacting molecules (see *Theory*), and (*b*) the chosen level of theory (*i.e.* the chosen *ansatz* for the XRW) fixes the electronic state of the system (when it is the case, even the excited state) that cannot be modified by the restraint to the observables. Therefore, the possibility of perturbing the 'starting' molecular wavefunction through the effects of an external field, or by means of intra- or inter-molecular orbital-interactions (all of them intrinsically included in the experimental data used as restraints) is not fully guaranteed. However, the previously reported results indicate that, at least in part, the XRW method is able to overcome the biases.

Having this in mind, one could easily imagine electron densities or molecular orbitals resulting from XRW computations as perfect candidates for the description of environment regions in fully quantum mechanical embedding calculations. As it is well known, embedding techniques are quantum chemistry strategies where the most important region of the investigated system is treated at a high level of theory, while the rest is described through a more approximate method. The most popular ones are certainly the multiscale QM/MM (quantum mechanics/molecular mechanics) approaches, which exploit a fully quantum mechanical technique to describe the crucial subunit and a molecular mechanics force field to deal with the remaining part of the system under exam (Warshel & Levitt, 1976; Field *et al.*, 1990; Gao, 1996; Senn & Thiel, 2009). However, in the last twenty years, many fully quantum mechanical embedding methods (Sun & Chan, 2016) were also devised and emerged as promising alternatives/complements to the well known QM/MM strategies. Just to cite some representative examples, we can mention the pioneering frozen density embedding theory (FDET) devised by Wesolowski and coworkers (Wesolowski & Warshel, 1993; Wesołowski, 2008; Wesolowski *et al.*, 2015), the projection-based embedding (PbE) approach jointly developed by the Manby and Miller research labs (Manby *et al.*, 2012; Barnes *et al.*, 2013; Lee *et al.*, 2019), and the multi-level techniques

introduced by Koch and collaborators (Saether *et al.*, 2017; Folkestad *et al.*, 2021; Marrazzini *et al.*, 2021). Among them, FDET optimizes the wavefunction of subsystem A in presence of the frozen electron density for the complementary subsystem B (where A+B gives the whole system). Following this philosophy, the Wesolowski technique has been recently coupled with the XRW method, in the sense that experimental electron density distributions resulting from preliminary XRW calculations were used for the first time to embed excited state computations for subsystems of interest (Ricardi *et al.*, 2020). This demonstrated that XRW densities are perfectly suitable for this purpose.

Prompted by this result, we decided to explore the possibility of using pre-determined X-ray restrained extremely localized molecular orbitals (XR-ELMOs) to profitably embed quantum mechanical calculations. To accomplish this task, we exploited the recently developed QM/ELMO (quantum mechanics/extremely localized molecular orbital) embedding approach (Macetti & Genoni, 2019, 2020, 2021*a*,*b*,*c*; Macetti *et al.*, 2020, 2021; Wieduwilt *et al.*, 2021). According to this technique, the chemically active region is treated in a fully quantum mechanical way, while the rest is described by means of transferred and frozen extremely localized molecular orbitals. In fact, due to their strict localization on small subunits (*i.e.* atoms, bonds or functional groups) ELMOs are orbitals that can be straightforwardly and reliably transferred from molecule to molecule (Genoni *et al.*, 2005, 2008; Sironi *et al.*, 2007, 2009; Meyer *et al.*, 2016*a*,*b*) and have been also assembled in proper libraries to describe all the possible elementary units of specific classes of compounds [*e.g.* natural amino acids or metal organic frameworks (MOFs)] (Meyer & Genoni, 2018; Wieduwilt, Macetti, Scatena *et al.*, 2021).

Initially developed only as Hartree–Fock/ELMO method (Genoni & Macetti, 2019), the QM/ELMO technique has been gradually extended to DFT (Macetti *et al.*, 2020), post-HF approaches (Macetti *et al.*, 2020; Macetti & Genoni, 2021*a*) and also strategies for the calculation of excited states (particularly, time-dependent density functional theory (TDDFT), equation-of-motion coupled cluster with single and double substitutions (EOM-CCSD), and initial maximum overlap method (IMOM)) (Macetti & Genoni, 2020; Macetti & Genoni, 2021*b*). As we will describe in detail in the next sections, in this work we considered the EOM-CCSD/ELMO and TDDFT/ELMO variants of the QM/ELMO approach (Macetti & Genoni, 2020), where, for the first time, instead of standard gas-phase ELMOs we exploited XR-ELMOs previously obtained using structure factor amplitudes associated with electron densities resulting from periodic *ab initio* calculations. The goal was twofold: (i) on the one hand, we wanted to check if the use of XR-ELMOs improves the QM/ELMO results introducing some features (*e.g.* ground state polarization of the environment) that are necessarily approximate in standard QM/ELMO calculations due to the frozen nature of the gas-phase embedding ELMOs; (ii) on the other hand, the investigation also represented another way of proving the capability of the XRW approach (and particularly of the XR-ELMO technique) in recovering crystal field effects.

The paper is organized as follows. In the next section we will briefly present the theory at the basis of the two methods that were extensively used in this study (namely, XR-ELMO and QM/ELMO techniques). In §3 we will provide all the details of the performed computations, while in §4 we will show and discuss the obtained results. In the last part of the paper, we will draw conclusions and outline future possibilities opened by this study.

2. Theory

2.1. X-ray restrained extremely localized molecular orbitals

In the X-ray restrained wavefunction (XRW) technique (Jayatilaka, 1998; Jayatilaka & Grimwood, 2001) one assumes to formally work with a fictitious molecular crystal in which each molecular unit does not interact with the other ones but having a global electron density that is equal to the one of the corresponding real interacting crystalline system. Furthermore, it is also assumed that all the units are described by independent wavefunctions that are formally identical and related to each other through the crystal symmetry operations, which will be hereafter indicated as roto-translations $\{\mathbf{Q}_k, \mathbf{q}_k\}_{k=1}^{N_m}$ (with N_m as the number of symmetry-equivalent positions in the crystal unit cell). Thanks to the previous assumptions, the global unit-cell electron density can be expressed as follows:

$$\rho_{\text{cell}}(\mathbf{r}) = \sum_{k=1}^{N_m} \rho_k(\mathbf{r}) = \sum_{k=1}^{N_m} \rho_0\left[\mathbf{Q}_k^{-1}(\mathbf{r} - \mathbf{q}_k)\right]. \tag{1}$$

In other words, the unit-cell electron density can be written only in terms of the electron density $\rho_0(\mathbf{r})$ corresponding to the reference crystal unit and, consequently, only in terms of the associated wavefunction $|\Psi_0\rangle$ for the reference unit. In the XRW approach, this wavefunction is not obtained by simply minimizing the electronic energy $E[\Psi_0]$ (where '$[\Psi_0]$' will hereinafter indicate the functional dependence on $|\Psi_0\rangle$), but minimizing the so-called Jayatilaka functional:

$$J[\Psi_0] = E[\Psi_0] + \lambda\left(\chi^2[\Psi_0] - \Delta\right), \tag{2}$$

where the second term on the right-hand side of the equation is the one that provides the restraints to the X-ray diffraction data (*i.e.* to the structure factor amplitudes) and that eventually guarantees that the global electron density of the assumed effective non-interacting system is identical to the global electron density of the corresponding crystal made of truly interacting molecules (see assumption above). λ is an external multiplier that modulates the weight of the external restraints and that is adjusted (*i.e.* not refined) during the XRW calculations, $\chi^2[\Psi_0]$ is the statistical distribution of the squared differences between the calculated and the experimental/theoretically generated structure factor amplitudes used as restraints, and Δ the desired agreement. Furthermore, we have that

$$\chi^2\left[\Psi_0\right]=\frac{1}{N_r-N_p}\sum_{\mathbf{h}}\frac{\left(\eta F_{\mathbf{h}}^{\rm calc}\left[\Psi_0\right]-F_{\mathbf{h}}^{\rm obs}\right)^2}{\sigma_{\mathbf{h}}^2}, \tag{3}$$

with N_r as the number of structure factor amplitudes, N_p the number of adjustable parameters, $\mathbf{h}$ the triad of Miller indices that label the reflection, η the h -independent scale-factor that puts the calculated structure factor amplitudes $\left\{F_{\mathbf{h}}^{\rm calc}\right\}$ on the same scale of the experimental/theoretically generated ones $\left\{F_{\mathbf{h}}^{\rm obs}\right\}$, and σ_h the experimental uncertainty associated with $F_{\mathbf{h}}^{\rm obs}$. When theoretically generated structure factor amplitudes are used as restraints, both $\sigma_{\mathbf{h}}$ and η are set equal to 1.0.

So far, we have not specified any functional form for the wavefunction $|\Psi_0\rangle$ that has to be determined. This choice defines the type of XRW method. In our case (XR-ELMO technique), the wavefunction for the reference crystal unit assumes the form of an ELMO wavefunction, which can be constructed by following the guidelines originally indicated by Stoll and coworkers (Stoll *et al.*, 1980). First, it is necessary to define a localization scheme that, according to chemical intuition, subdivides the system under exam into fragments that may overlap. In most cases, this localization pattern coincides with the Lewis structure of the investigated molecule. After this step, a local basis-set $\Omega_i=\left\{\left|\chi_\mu^i\right\rangle\right\}_{\mu=1}^{M_i}$ is automatically assigned to each subunit into which we have initially fragmented the examined system. These local basis-sets are constituted by the only M_i basis functions centred on the atoms that belong to the subunits and are used to expand the molecular orbitals corresponding to the different fragments. For example, for a generic fragment i, the γth occupied ELMO can be expressed as follows:

$$\left|\varphi_\gamma^i\right\rangle=\sum_{\mu\in\Omega_i}C_{\mu\gamma}^i\left|\chi_\mu^i\right\rangle. \tag{4}$$

This means that, for the molecular orbitals of fragment i, only the coefficients corresponding to the basis functions belonging to basis-set Ω_i will be different from zero and, consequently, these orbitals will be strictly localized on that subunit, without tails that extend to other fragments.

The molecular orbitals defined by equation (4) are those that are used to construct the ELMO wavefunction, namely the single Slater determinant that, for a *2N*-electron closed-shell system, can be expressed like this:

$$\left|\Psi_0\right\rangle=\frac{1}{[(2N)!]^{1/2}\det[\mathbf{S}]}\hat{A}\left[\prod_{i=1}^{f}\prod_{\gamma=1}^{n_i}\varphi_\gamma^i\overline{\varphi_\gamma^i}\right], \tag{5}$$

where $\hat{A}$ is the usual antisymmetrizer, f is the number of fragments into which the system has been preliminarily subdivided, n_i is the number of occupied ELMOs for the ith subunit, $\varphi_{i\gamma}$ is the generic γth occupied ELMO for fragment i, and $\mathbf{S}$ is the overlap matrix of the occupied ELMOs due to the non-orthogonality of the extremely localized molecular orbitals. For the sake of completeness, the overline symbol indicates a spin orbital with spin-part β, whereas its absence denotes a spin orbital with spin-part α.

In the context of the XR-ELMO approach, the coefficients that expand the ELMOs according to equation (4) are obtained by finding those extremely localized molecular orbitals that variationally minimize the Jayatilaka functional given by equation (2). If now we define the total scattering operator for a *2N*-electron system as

$$\begin{aligned}\hat{\mathfrak{J}}&=\sum_{j=1}^{2N}\sum_{k=1}^{N_m}\exp\left[i2\pi\left(\mathbf{Q}_k\mathbf{r}_j+\mathbf{q}_k\right)\cdot\left(\mathbf{Gh}\right)\right]\\&=\sum_{j=1}^{2N}\hat{I}_{\mathbf{h}}(\mathbf{r}_j)=\sum_{j=1}^{2N}\hat{I}_{\mathbf{h},R}(\mathbf{r}_j)+i\hat{I}_{\mathbf{h},C}(\mathbf{r}_j),\end{aligned} \tag{6}$$

with $\mathbf{G}$ as the reciprocal lattice matrix, it is possible to show that the variational minimization reduces to the self-consistent field (SCF) resolution of the following modified Hartree–Fock equations for each fragment (Genoni, 2013*a*,*b*; Genoni & Meyer, 2016):

$$\hat{F}^{i,\rm XRW}\left|\varphi_\gamma^i\right\rangle=\varepsilon_\gamma^i\left|\varphi_\gamma^i\right\rangle. \tag{7}$$

where the new modified Fock operator for the generic ith subunit, $\hat{F}^{i,\rm XRW}$, is given by

$$\begin{aligned}\hat{F}^{i,\rm XRW}&=(1-\hat{\rho}+\hat{\rho}^{i\dagger})\hat{F}(1-\hat{\rho}+\hat{\rho}^i)\\&+\lambda\sum_{\mathbf{h}}K_{\mathbf{h}}{\rm Re}\left\{F_{\mathbf{h}}^{\rm calc}\right\}(1-\hat{\rho}+\hat{\rho}^{i\dagger})\hat{I}_{\mathbf{h},R}(1-\hat{\rho}+\hat{\rho}^i)\\&+\lambda\sum_{\mathbf{h}}K_{\mathbf{h}}{\rm Im}\left\{F_{\mathbf{h}}^{\rm calc}\right\}\left(1-\hat{\rho}+\hat{\rho}^{i\dagger}\right)\hat{I}_{\mathbf{h},C}(1-\hat{\rho}+\hat{\rho}^i)\end{aligned} \tag{8}$$

with $\hat{\rho}$ as the global density operator (which depends on all the occupied ELMOs and couples the eigenvalue equations for the different fragments), with $\hat{\rho}^i$ as the density operator for subunit i (which depends only on the occupied ELMOs localized on the fragment), and with

$$K_{\mathbf{h}}=\frac{2\eta}{N_r-N_p}\frac{\eta F_{\mathbf{h}}^{\rm calc}-F_{\mathbf{h}}^{\rm obs}}{\sigma_{\mathbf{h}}^2F_{\mathbf{h}}^{\rm calc}}. \tag{9}$$

When $\lambda=0$, the Jayatilaka functional [namely, equation (2)] simply corresponds to the electronic energy of the system and, therefore, equations (7) and (8) revert to the standard Stoll equations for the determination of unrestrained (*i.e.* gas-phase) ELMOs (Stoll *et al.*, 1980; Fornili *et al.*, 2003).

The ELMO and XR-ELMO techniques were implemented in a modified version of the *GAMESS-UK* quantum chemistry suite of programs (Guest *et al.*, 2005). This software was used for all the unrestrained ELMO and XR-ELMO computations performed in this investigation.

2.2. QM/ELMO embedding technique

The first step of the QM/ELMO method consists in the subdivision of the investigated system into QM and ELMO regions, with the former corresponding to the chemically crucial subsystem and the latter representing the chemical environment. Afterwards, the ELMOs are transferred to the ELMO subunit from suitable model molecules or from the recently constructed libraries (Meyer & Genoni, 2018).

Before the real QM/ELMO calculations, it is necessary to perform a preliminary orthogonalization procedure that involves both the exported ELMOs and the basis functions

centred on the atoms of the QM region. This procedure entails three different steps: (i) Löwdin orthogonalization of the transferred ELMOs; (ii) orthogonalization of the QM basis functions against the Löwdin orthogonalized ELMOs (in other words, the orthonormalized ELMOs are projected out of the original QM basis functions); (iii) canonical orthogonalization of the QM basis functions resulting from point (ii). The three previous steps can be summarized through the following matrix transformation:

$$\boldsymbol{\chi}' = \boldsymbol{\chi}\mathbf{B}, \tag{10}$$

where $\boldsymbol{\chi} = [|\chi_1\rangle, |\chi_2\rangle, \ldots, |\chi_M\rangle]$ is the $1 \times M$ array of the M original non-orthogonal basis functions of the whole system (QM+ELMO regions), $\boldsymbol{\chi}' = \left[\left|\chi'_1\right\rangle, \left|\chi'_2\right\rangle, \ldots, \left|\chi'_{M_{\rm QM}}\right\rangle\right]$ is the $1 \times M_{\rm QM}$ array of the $M_{\rm QM}$ final orthonormal basis functions for the QM subunit (with $M_{\rm QM} \ll M$), and $\mathbf{B}$ is an $M \times M_{\rm QM}$ transformation matrix that is fundamental for the QM/ELMO SCF algorithm (see below). Interested readers can find more details about the orthogonalization procedure and about the construction of matrix $\mathbf{B}$ in the original papers of the QM/ELMO technique (Macetti & Genoni, 2019; Macetti *et al.*, 2020).

After the orthogonalizations, the SCF procedure starts. It is summarized by the following points:

(1) Construction of the Fock matrix $\mathbf{F}$ using the original basis functions $\boldsymbol{\chi}$.

(2) Transformation of the Fock matrix to the set $\boldsymbol{\chi}'$ of the orthonormal basis functions for the QM subsystem by exploiting matrix $\mathbf{B}$: $\mathbf{F}' = \mathbf{B}^{\dagger}\mathbf{F}\mathbf{B}$ (note that we pass from an $M \times M$ matrix to a reduced $M_{\rm QM} \times M_{\rm QM}$ matrix).

(3) Diagonalization of matrix $\mathbf{F}'$: $\mathbf{F}'\mathbf{C}' = \mathbf{C}'\mathbf{E}'$.

(4) Transformation of the molecular orbitals to the set $\boldsymbol{\chi}$ of the original basis functions: $\mathbf{C} = \mathbf{B}\mathbf{C}'$.

(5) Computation of the one-electron density matrix for the quantum mechanical region: $\mathbf{P}^{\rm QM} = \mathbf{C}\mathbf{C}^{\dagger}$.

(6) Check of convergence on energy and density matrix: if convergence is achieved, the SCF procedure halts; otherwise, the cycle restarts from point 1 with the update of the Fock matrix $\mathbf{F}$ using the density matrix $\mathbf{P}^{\rm QM}$ obtained at the previous point.

The previous SCF cycle is the preliminary step to perform post-HF/ELMO calculations or QM/ELMO calculations for excited states. In fact, the SCF procedure provides occupied and virtual molecular orbitals that are necessary for this kind of computations. For a $2N$-electron closed-shell QM subsystem, the diagonalization of the reduced matrix $\mathbf{F}'$ (point 3 of the SCF cycle) gives N occupied molecular orbitals ($N \ll N + N_{\rm ELMO}$) and $M_{\rm QM} - N$ virtual molecular orbitals ($M_{\rm QM} - N \ll M - N$), with these reductions in the number of molecular orbitals that were shown to be crucial in order to significantly lowering the computational costs (Macetti *et al.*, 2020; Macetti & Genoni, 2020).

So far, the QM/ELMO calculations have been exclusively performed using ELMOs preliminarily obtained from gas-phase computations. As already explained above, these ELMOs are transferred to the ELMO region and are kept frozen throughout the QM/ELMO calculation. In other words, they are not affected at all by the environment (including the QM region). In this work, for the first time, we will try to slightly improve this approximation by describing the ELMO subsystem through XR-ELMOs. In fact, as we will see in the next section in more details, these orbitals are determined through XRW computations and, at least partially, they already take into account the effects of the environment.

For the sake of completeness, all the current variants of the QM/ELMO approach were implemented in an in-house modified version of the quantum chemistry package *Gaussian09* (Frisch *et al.*, 2009), which was therefore used to carry out all the QM/ELMO calculations of this study.

3. Computational details

To test the performances of QM/ELMO calculations with X-ray restrained ELMOs, we considered an experimental crystal structure of acrylamide (Zhou *et al.*, 2007). After the elongation of the bond lengths involving hydrogen atoms to the tabulated values of Allen & Bruno (2010), we exploited the adjusted crystal structure [see the graphical representation of the unit cell in Fig. 1(*a*)] to perform single-point periodic *ab initio* calculations (*i.e.* periodic calculations with fixed geometry and cell parameters) at different levels of theory: Hartree–Fock, DFT-M06-HF and DFT-M06-2X, all of them with the cc-pVDZ basis-set. All these computations were carried out using the *CRYSTAL14* package (Dovesi, Orlando *et al.*, 2014; Dovesi, Saunders *et al.*, 2014). Always adopting the above-indicated levels of theory and basis-set, we also carried out periodic calculations exploiting the MOLSPLIT option that allowed us to turn off the mutual interactions between molecules in the crystal. From all the previous computations

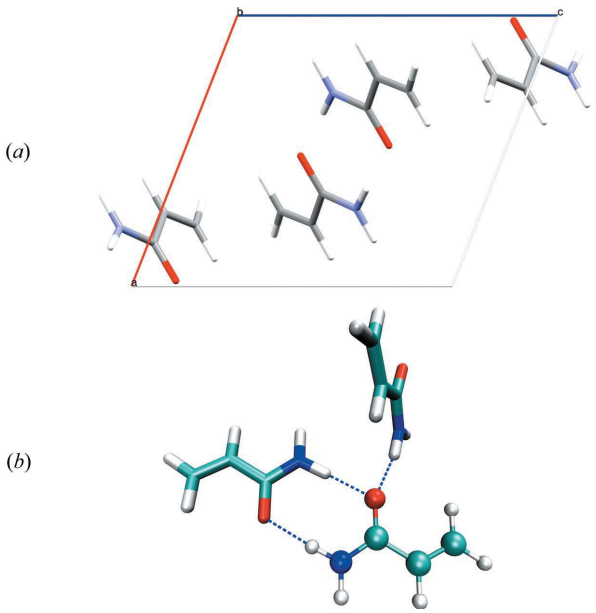

Figure 1
(*a*) Unit cell of the acrylamide crystal structure; (*b*) acrylamide trimer extracted from the crystal structure and used in the QM/ELMO calculations: QM and ELMO regions in ball and stick, and liquorice representations, respectively.

we also obtained all the possible theoretical structure factor amplitudes compatible with the considered crystal structure up to a resolution of 1.25 Å^{-1}.

Using the theoretical structure factor amplitudes, we afterwards performed XR-ELMO computations. As already reminded in the *Introduction*, in previous studies it was observed that the capability of the XRW method in capturing crystal field and electron correlation effects importantly depends on the resolution of the X-ray data used as external restraints (Ernst *et al.*, 2020; Genoni *et al.*, 2017). Noteworthy, these effects are best recovered when medium/low-resolution datasets are exploited in the computations. Therefore, we considered four different resolution shells (expressed in $\sin\theta/\lambda$) for the XR-ELMO calculations: 1.25 Å^{-1}, 1.00 Å^{-1}, 0.75 Å^{-1} and 0.50 Å^{-1}. Using these sets of structure factor amplitudes for each level of theory (including the MOLSPLIT variants), we then carried out XR-ELMO computations (overall, 24 distinct XR-ELMO computations) varying the external multiplier λ from 0.0 to 10.0 with a λ step of 0.5. In addition to these XR-ELMO calculations, we also performed a standard gas-phase ELMO computation on the molecular geometry extracted from the experimental crystal structure, always with the element–hydrogen bond lengths adjusted according to the Allen & Bruno (2010) tabulated values. All the ELMO and XR-ELMO calculations described in this paragraph were performed using the cc-pVDZ basis-set and with a localization scheme corresponding to the Lewis structure for the acrylamide molecule.

The gas-phase ELMOs and the XR-ELMOs were afterwards exploited in EOM-CCSD/ELMO and TDDFT/ELMO computations (see below for more details). The (XR-)ELMOs were transferred to the ELMO region through the *ELMOdb* program associated with the ELMO libraries, which implements the strategy originally devised by Philipp and Friesner for the rotation/transfer of strictly localized bond orbitals (Philipp & Friesner, 1999; Meyer *et al.*, 2016*a*).

For the EOM-CCSD/ELMO and TDDFT/ELMO computations (Macetti & Genoni, 2020), we considered an acrylamide trimer [see Fig. 1(*b*)] extracted from the adjusted experimental crystal structure: the reference crystal unit was considered as our QM region, while the ELMO subsystem consisted of the two acrylamide molecules establishing direct hydrogen bond interactions with the chromophore centre of the reference unit [see again Fig. 1(*b*)]. Therefore, it is worth specifying that, in this study, the two surrounding acrylamide units were simply considered as spectators, namely we considered them as environment subunits not directly involved in the examined electronic transitions. Furthermore, all the EOM-CCSD/ELMO and TDDFT/ELMO calculations were performed with all the sets of (XR-)ELMOs resulting from the previously described (XR-)ELMO computations (all possible combinations of level of theory, resolution and λ values). In all situations, we adopted the cc-pVDZ basis-set and we computed the excitation energies associated with the first two electronic transitions of the investigated system. For the TDDFT/ELMO calculations, the CAM-B3LYP functional was used to treat the quantum mechanical region.

As reference values, we considered the excitation energies for the first two excited states resulting from *in vacuo* EOM-CCSD and TDDFT (CAM-B3LYP) computations on the isolated acrylamide molecule (cc-pVDZ basis set). The large spectrum of performed EOM-CCSD/ELMO and TDDFT/ELMO calculations allowed us to evaluate the effect of different parameters on the QM/ELMO results: (i) the resolution of the structure factor amplitudes used as external restraints in the calculations of the XR-ELMOs afterwards employed for the embedding; (ii) the external multiplier λ used in the XR-ELMO computations; (iii) the level of theory chosen in the periodic calculations for the generation of the structure factor amplitudes employed as external restraints.

4. Results and discussion

In this section, we will mainly show and discuss the variations ΔE_{ex} of the excitation energies associated with the first two excited states of acrylamide with respect to the corresponding gas-phase values. These variations were determined considering the results of EOM-CCSD/ELMO and TDDFT/ELMO computations where the environment was described by means of unrestrained (*i.e.* gas-phase) or XR-ELMOs.

Let us first consider Fig. 2. We reported the ΔE_{ex} values obtained through EOM-CCSD/ELMO computations that exploited XR-ELMOs resulting from the XRW fitting (λ = 10.0) of sets of structure factor amplitudes associated with the

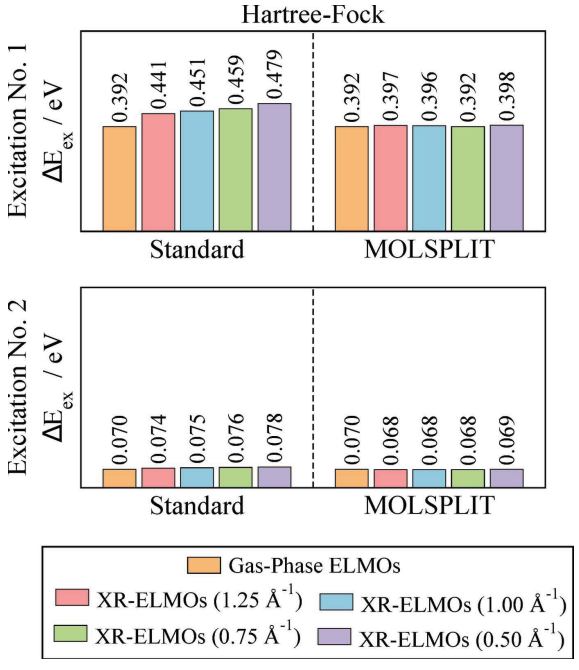

Figure 2
Variations of the excitation energies (ΔE_{ex}) for the first two excited states of acrylamide with respect to the corresponding gas-phase values, as resulting from EOM-CCSD/ELMO calculations with embedding gas-phase ELMOs and with embedding XR-ELMOs obtained through XRW fittings (λ = 10.0) of X-ray datasets associated with periodic Hartree–Fock densities (standard and MOLSPLIT) and characterized by different maximal resolutions (1.25 Å^{-1}, 1.00 Å^{-1}, 0.75 Å^{-1} and 0.50 Å^{-1}).

periodic Hartree–Fock density and characterized by different resolutions. Analogous results based on the periodic M06-HF and M06-2X electron distributions are respectively shown in Figs. S1 and S2 in the supporting information. For the sake of comparison, in all the above-mentioned figures we also showed the variation of the excitation energy that we obtained when simple gas-phase ELMOs were used to describe the environment of the chromophore centre. Hereinafter, the differences with respect to the ΔE_{ex} values obtained through QM/ELMO calculations with embedding gas-phase ELMOs will be also indicated as $\Delta\Delta E_{ex}$ increments.

Concerning the first excited state (see top panels of Fig. 2), we can observe that the unrestrained (*i.e.* the gas-phase) ELMOs already account for a significant blue-shift (0.392 eV) of the excitation energy, which can be explained with the fact that intermolecular interactions are mostly described through the embedding scheme of the QM/ELMO method. At the same time, we can also notice that ΔE_{ex} further increases when the embedding of the QM region is provided by XR-ELMOs resulting from the fitting of X-ray data associated with the standard (*i.e.* non-MOLSPLIT) periodic Hartree–Fock electron density distribution. However, the $\Delta\Delta E_{ex}$ increments are small. We can consider these increments as first-order corrections to the blue shift of the excitation energy that we already have when only traditional unrestrained ELMOs are used to describe the environment. This can be explained bearing in mind that the XRW technique effectively allows us to capture the effects of intermolecular interactions on the electron density. Owing to this property, the XR-ELMOs resulting from XRW calculations polarize due to the presence of the ground state electron distributions of the other molecular units in the crystal, and, for this reason, the $\Delta\Delta E_{ex}$ increments observed in Fig. 2 can be considered as ground state polarization corrections to the blue-shift of the excitation energy determined through gas-phase extremely localized molecular orbitals. As one should expect, in Fig. 2 we can also observe that when we use XR-ELMOs resulting from MOLSPLIT periodic electron densities, the obtained $\Delta\Delta E_{ex}$ increments are negligible, with all the ΔE_{ex} variations of the excitation energy with respect to the gas-phase value practically almost equivalent to the one resulting from the EOM-CCSD/ELMO calculation with unrestrained ELMOs. This is clearly related to the fact that the MOLSPLIT option in the periodic *ab initio* calculations turned off all the intermolecular interactions. Therefore, the XR-ELMOs resulting from the fitting of MOLSPLIT structure factor amplitudes do not include the above-mentioned ground state polarization effects. Completely analogous results were obtained also for the M06-HF and M06-2X levels of theory (see Figs. S1 and S2 in the supporting information).

To conclude the analysis of the results obtained for the first excited state, we can also see that, for the standard results, the $\Delta\Delta E_{ex}$ increments systematically increase as we consider lower resolutions for the X-ray data exploited in the computation of the embedding XR-ELMOs. This is valid for all the levels of theory of the underlying periodic electron distributions (see again Figs. 2, S1 and S2) and is in full agreement with the outcomes of previous investigations, according to which the XRW approach better captures electron correlation and crystal fields effects on the electron density when only low/medium-angle structure factor amplitudes are used as external restraints. This can be explained by reconsidering the expression of the χ^2 statistical agreement [see equation (3)] and, at the same time, analysing the differences between standard and MOLSPLIT structure factor amplitudes (hereinafter also simply indicated as $F_{\mathbf{h}}^{cryst}$ and $F_{\mathbf{h}}^{gas}$, respectively) as a function of $\sin\theta/\lambda$. As we can see in Fig. 3, regardless of the chosen level of theory, the differences between the $F_{\mathbf{h}}^{cryst}$ and $F_{\mathbf{h}}^{gas}$ values are very small for high-angle reflections, which agrees with the fact that crystal field effects are not expected to modify the core electrons distribution. At low resolution, instead there are larger discrepancies (not unexpected because of the larger amplitudes) and a non-uniform distribution of the mean deviation. Therefore, the largest differences are observed at low/medium angle, namely for those structure factors associated with the valence electron density, which is the most affected by intermolecular interactions. We can also notice that reflections are not evenly distributed in resolution shells and, above all, that high-angle reflections are by far more numerous than the low-angle ones. Therefore, the contribution of the less important (in terms of information about the crystal field effects) high-angle reflections becomes predominant in equation (3) for datasets of structure factor amplitudes characterized by $\sin\theta/\lambda \leq 1.25$ Å^{-1} or $\sin\theta/\lambda \leq 1.00$ Å^{-1}, thus down-weighting the low/medium-angle reflections that contain most of the information about the influence of the crystal environment. Consequently, the recovery of the

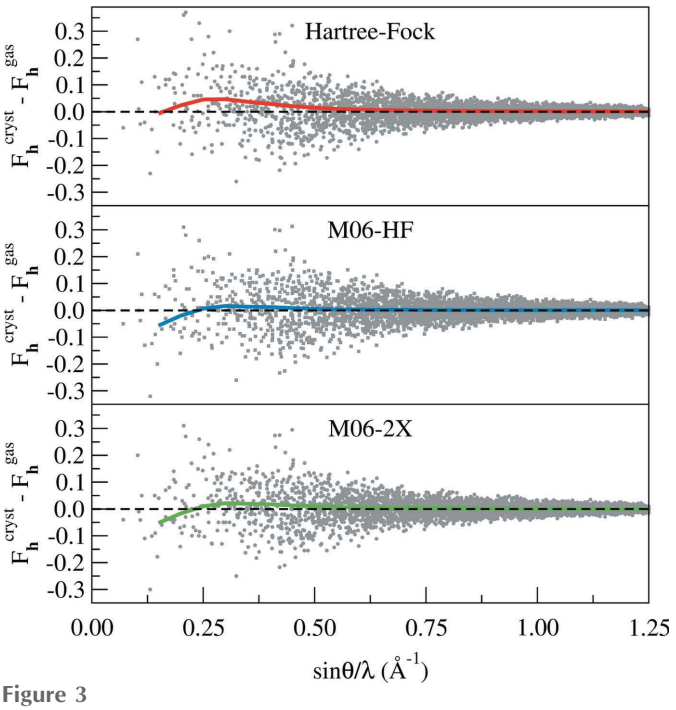

Figure 3
Discrepancies between the standard and MOLSPLIT structure factor amplitudes ($F_{\mathbf{h}}^{cryst}$ and $F_{\mathbf{h}}^{gas}$, respectively) at different levels of theory. The solid curves show the trends of the average discrepancy as a function of $\sin\theta/\lambda$.

crystal field effects is larger only when high-angle reflections are neglected, namely using X-ray datasets with at least $\sin\theta/\lambda \leq 0.75$ Å^{-1}. This explains why in the top panels of Figs. 2, S1 and S2 we observe larger $\Delta\Delta E_{ex}$ increments when we use embedding XR-ELMOs resulting from XRW calculations that exploit datasets of structure factor amplitudes of lower resolution.

In the bottom panel of Fig. 2, we have reported the ΔE_{ex} variations obtained through all our EOM-CCSD/ELMO calculations for the second excited state of acrylamide. Unlike the first electronic excitation, in this case we obtained $\Delta\Delta E_{ex}$ increments that are quite small also when we used embedding XR-ELMOs resulting from the fitting of structure factor amplitudes associated with the standard periodic Hartree–Fock electron density (namely, the non-MOLSPLIT Hartree–Fock electron density). Similar results were also observed for the M06-HF and M06-2X cases (see Figs. S1 and S2). To explain the different trends, we must consider the character of the two excited states. To accomplish this task, we have determined the natural transition orbitals (NTOs) associated with the first and second electronic transitions (see Fig. 4), as resulting from the gas-phase EOM-CCSD calculation on acrylamide. From the NTO analysis we can clearly see that the first excited state (S1) has an $n \rightarrow \pi^*$ nature, while the second one (S2) is a $\pi \rightarrow \pi^*$ transition. Therefore, while the first excited state involves the lone pairs of the oxygen atom and is consequently influenced by the intermolecular interactions in the considered acrylamide trimer [see again Fig. 1(*b*)], the second excited state implicates only π molecular orbitals that are only marginally influenced by the hydrogen-bond network of the investigated system. This explains why our EOM-CCSD/ELMO computations with XR-ELMOs provided $\Delta\Delta E_{ex}$ increments for the first $n \rightarrow \pi^*$ electronic transition that are larger than those for the second $\pi \rightarrow \pi^*$ excited state.

For the sake of brevity, we reported the results of our TDDFT/ELMO calculations in Figs. S3–S5. They are analogous to the EOM-CCSD/ELMO ones, namely: (i) the use of embedding XR-ELMOs allowed the introduction of first-order corrections ($\Delta\Delta E_{ex}$ increments) to the ΔE_{ex} blue shift of the excitation energy of the first excited state obtained through TDDFT/ELMO calculations with gas-phase ELMOs; (ii) the $\Delta\Delta E_{ex}$ increments become larger as we use XR-ELMOs resulting from XRW fittings of lower-resolution datasets of structure factor amplitudes; (iii) TDDFT/ELMO calculations with XR-ELMOs corresponding to MOLSPLIT electron densities provide negligible $\Delta\Delta E_{ex}$ values; (iv) $\Delta\Delta E_{ex}$ increments are small but non-negligible for the first excited state, while they are almost unimportant for the second electronic transition, which is again related to the different character of the excited states (see the corresponding NTO analysis shown in Fig. S6).

We will now briefly discuss the variation of our QM/ELMO results as a function of the values of the external parameter λ that were used in the X-ray restrained wavefunction fitting calculations of the embedding XR-ELMOs. As is well known, the determination of the best λ value at which terminating the XRW fitting calculations is still an unsolved problem. When experimental diffraction data are used, one should possibly stop the computations at the value of λ for which the χ^2 statistical agreement is equal to or starts being lower than 1.0, in such a way that the calculated structure factor amplitudes are on average within one standard deviation of the experimental values. This is not always possible, and, above all, this is never the case when the external restraints are given by theoretically generated structure factor amplitudes (χ^2 already lower than 1.0 at $\lambda = 0.0$). In those situations, it is at least necessary that a sort of plateau is reached for the χ^2 statistical agreement or for a property of interest.

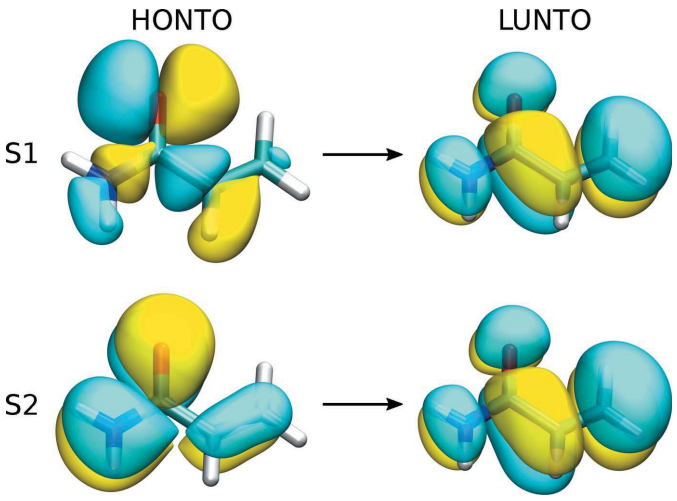

Figure 4
HONTOs (highest occupied natural transition orbitals) and LUNTOs (lowest unoccupied natural transition orbitals) associated with the first and the second excited states of acrylamide (here labelled as S1 and S2, respectively), as resulting from the gas-phase calculation at EOM-CCSD level with basis-set cc-pVDZ; all the isosurfaces set to 0.02 a.u.

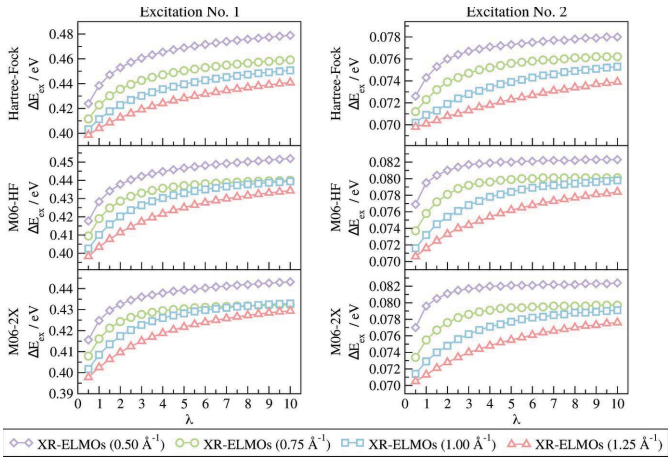

Figure 5
Variations of the excitation energies (ΔE_{ex}) for the first two excited states of acrylamide with respect to the corresponding gas-phase values, as obtained through EOM-CCSD/ELMO calculations with embedding XR-ELMOs. The variations are reported as a function of the λ value used in the preliminary calculations of the embedding XR-ELMOs at different resolutions (1.25 Å^{-1}, 1.00 Å^{-1}, 0.75 Å^{-1} and 0.50 Å^{-1}) and levels of theory (standard Hartree–Fock, M06-HF and M06-2X).

As mentioned in §3, in all our XR-ELMO calculations λ varied from 0 to 10.0 with a step of 0.5. In Fig. 5, for each level of theory of the underlying standard periodic electron densities and for each set of X-ray structure factor amplitudes exploited in the computations of the XR-ELMOs, we plotted ΔE_{ex} as a function of λ for all our EOM-CCSD/ELMO calculations on the first and second excited states of acrylamide. We can observe that, independently of the level of theory and of the resolution of the structure factor amplitudes dataset used as external restraints, a plateau in ΔE_{ex} is practically always reached, thus showing a sort of convergence in our QM/ELMO calculations of the acrylamide excited states. Furthermore, in a different way, we can appreciate again the dependence of the results on the resolution of the employed X-ray datasets. In fact, it is possible to see that the largest $\Delta\Delta E_{ex}$ increments (namely the variations of ΔE_{ex} with respect to the unrestrained value at $\lambda = 0.0$) are always observed for the EOM-CCSD/ELMO calculations exploiting embedding XR-ELMOs obtained with the X-ray datasets with $\sin\theta/\lambda \leq 0.50$ Å^{-1}. On the contrary, the smallest ones correspond to the EOM-CCSD/ELMO computations performed with XR-ELMOs obtained with the largest set of structure factor amplitudes ($\sin\theta/\lambda \leq 1.25$ Å^{-1}). It is worth noting that in Fig. 5 we can observe the dependence on the resolution also in the case of the second $\pi \rightarrow \pi^*$ excited state, which could not be completely appreciated in Figs. 2, S1 and S2 due to the small values of the $\Delta\Delta E_{ex}$ increments. For the corresponding TDDFT/ELMO calculations we obtained completely analogous results, which were reported in Fig. S7.

Now, we will analyse the dependence of the results on the level of theory of the preliminary periodic *ab initio* calculations. The values resulting from our EOM-CCSD/ELMO computations are shown in Fig. 6, where we reported the ΔE_{ex} variations obtained at different levels of theory (both standard and MOLSPLIT), for two resolutions of the X-ray datasets (0.50 Å^{-1} and 0.75 Å^{-1}) and again for the first two excited states.

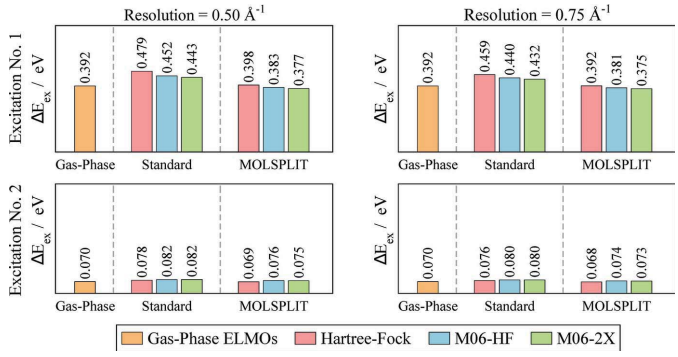

Figure 6
Variations of the excitation energies (ΔE_{ex}) for the first two excited states of acrylamide with respect to the corresponding gas-phase values, as resulting from EOM-CCSD/ELMO calculations with embedding gas-phase ELMOs and with embedding XR-ELMOs obtained through XRW fittings ($\lambda = 10.0$) of structure factor amplitudes computed at different levels of theory (Hartree–Fock, M06-HF, M06-2X, MOLSPLIT-Hartree–Fock, MOLSPLIT-M06-HF and MOLSPLIT-M06-2X). The results are shown for two resolutions of the X-ray datasets (0.50 Å^{-1} and 0.75 Å^{-1}).

Concerning the first $n \rightarrow \pi^*$ electronic transition (top panel of Fig. 6) we can observe that, when intermolecular interactions are included (standard case), the largest $\Delta\Delta E_{ex}$ increments are observed at Hartree–Fock level, while the EOM-CCSD/ELMO calculations based on XR-ELMOs associated with the M06-2X and M06-HF periodic densities provided lower and similar variations.

However, it is worth noting that, in all the observed $\Delta\Delta E_{ex}$ increments for the first excited state, we do not only have the effects due to the intermolecular interactions. In the Hartree–Fock case we must also include the so-called localization error because ELMOs are orbitals strictly localized on small molecular subunits and in the XR-ELMO calculations they were fitted to structure factor amplitudes associated with an electron density obtained from completely delocalized molecular orbitals (*i.e.* the Hartree–Fock MOs). In the M06-2X increments, in addition to the localization error, we have the exchange-correlation effects on the electron density due to the use of the approximate exchange-correlation functional M06-2X in the periodic computations. Finally, in the M06-HF results we have the localization error and purely correlation effects, but not exchange effects because in functional M06-HF we have 100% Hartree–Fock exact exchange, which is the same treatment of exchange that we have in the unrestrained (gas-phase) ELMO calculations. To evaluate the extent of the above-mentioned contributions, we can consider the results of the MOLSPLIT-based calculations, where the effects of the intermolecular interactions are turned off. We can see that, in the MOLSPLIT case, the $\Delta\Delta E_{ex}$ increments are completely negligible (Hartree–Fock results) or much smaller (M06-HF and M06-2X) than those observed in the standard non-MOLSPLIT situation. This indicates that, for the first $n \rightarrow \pi^*$ electronic transition, the effects due to the intermolecular interactions overwhelm the others.

Let us consider the results obtained for the second $\pi \rightarrow \pi^*$ excited state (bottom panel of Fig. 6). As expected and as already discussed above, for all the levels of theory the $\Delta\Delta E_{ex}$ increments are very small. Furthermore, from the MOLSPLIT results it is possible to observe that a large part of those increments is generally due to other effects besides intermolecular interactions, thus indicating that the $\pi \rightarrow \pi^*$ electronic transition is indeed only marginally affected by the hydrogen-bond network present in the considered acrylamide trimer.

Similar results were obtained also through the corresponding TDDFT/ELMO calculations. For the sake of completeness, they are shown in Fig. S8.

5. Conclusions

In this work, we performed QM/ELMO calculations of excited states (particularly EOM-CCSD/ELMO and TDDFT/ELMO computations) where, for the first time, X-ray restrained extremely localized molecular orbitals have been used to describe the external environment region. The XR-ELMOs have been preliminarily obtained through XRW fittings of

X-ray structure factor amplitudes associated with electron densities resulting from periodic *ab initio* calculations.

Although in QM/ELMO calculations a large part of the effects due to intermolecular interactions can be already described by means of gas-phase ELMOs, the results obtained in this work have shown that, thanks to the use of embedding XR-ELMOs, we can also automatically include ground state polarization effects. This is possible due to the efficiency of the XRW approach in including the effects of the crystal field on the electron density. However, it is also worth noting that the above-mentioned corrections for ground state polarization are effectively introduced only in case of (excited) states that are significantly influenced by the intermolecular interaction effects captured by the embedding XR-ELMOs used in the QM/ELMO calculations. In our work, this was the case of the first $n \rightarrow \pi^*$ electronic transition involving the oxygen atom lone pairs, which clearly play a role in the hydrogen-bond network of the investigated system.

Moreover, in agreement with previous studies, the outcomes of our computations indicated again that the effects related to intermolecular interactions in the crystal are best captured when medium/low-resolution X-ray datasets are exploited in the XRW computations. This was particularly evinced by observing that the largest variations of the excitation energies with respect to the corresponding gas-phase values were obtained when the reduced 0.50 Å^{-1} X-ray dataset was used for the determination of the embedding XR-ELMOs, while the smallest deviations were noticed with the highest-resolution set among those that were considered (1.25 Å^{-1}).

Therefore, in addition to proving again the efficiency of the XRW technique in capturing crystal field effects on the electron densities, the results of this investigation showed that X-ray restrained electron distributions and molecular orbitals can be profitably used in fully quantum mechanical embedding calculations. In fact, this kind of electron densities and molecular orbitals are already polarized and can therefore automatically include effects that we can only introduce through *a posteriori* corrections when traditional gas-phase electron distributions or orbitals are used. We thus envisage future extensions of the existing ELMO libraries (Meyer & Genoni, 2018) by including XR-ELMOs associated with experimental or periodic *ab initio* electron density distributions. This will be useful not only to perform more accurate theoretical QM/ELMO embedding calculations, but also to improve the results of structural refinements carried out through the recently proposed HAR-ELMO technique (Malaspina *et al.*, 2019), which combines the well known Hirshfeld atom refinement (HAR) approach (Jayatilaka & Dittrich, 2008; Capelli *et al.*, 2014; Kleemiss *et al.*, 2021) with the ELMO databanks.

Finally, thanks to the further confirmation that crystal field effects can be effectively and automatically grasped through XRW calculations, we believe that in the future the Jayatilaka technique could be successfully exploited also for the development of new families of DFT functionals targeting the proper description of intermolecular interactions.

Acknowledgements

AG and GM gratefully thank Fabien Pascale for the set-up and maintenance of the LPCT cluster, which was used to perform most of the calculations reported in this paper.

Funding information

The following funding is acknowledged: Agence Nationale de la Recherche (grant No. ANR-17-CE29-0005-01). The High-Performance Computing Center *EXPLOR* of the University of Lorraine is also acknowledged for providing computing time through the projects 2019CPMXX0966, 2019CPMXX0886 and 2019CPMXX1332.

References

Allen, F. H. & Bruno, I. J. (2010). *Acta Cryst.* B**66**, 380–386.
Barnes, T. A., Goodpaster, J. D., Manby, F. R. & Miller, T. F. III (2013). *J. Chem. Phys.* **139**, 024103.
Bučinský, L., Jayatilaka, D. & Grabowsky, S. (2016). *J. Phys. Chem. A*, **120**, 6650–6669.
Bytheway, I., Grimwood, D. J., Figgis, B. N., Chandler, G. S. & Jayatilaka, D. (2002). *Acta Cryst.* A**58**, 244–251.
Bytheway, I., Grimwood, D. J. & Jayatilaka, D. (2002). *Acta Cryst.* A**58**, 232–243.
Capelli, S. C., Bürgi, H.-B., Dittrich, B., Grabowsky, S. & Jayatilaka, D. (2014). *IUCrJ*, **1**, 361–379.
Casati, N., Genoni, A., Meyer, B., Krawczuk, A. & Macchi, P. (2017). *Acta Cryst.* B**73**, 584–597.
Cole, J. M. & Hickstein, D. D. (2013). *Phys. Rev. B*, **88**, 184105.
Dos Santos, L. H. R., Genoni, A. & Macchi, P. (2014). *Acta Cryst.* A**70**, 532–551.
Dovesi, R., Orlando, R., Erba, A., Zicovich-Wilson, C. M., Civalleri, B., Casassa, S., Maschio, L., Ferrabone, M., De La Pierre, M., D'Arco, P., Noël, Y., Causà, M., Rérat, M. & Kirtman, B. (2014). *Int. J. Quantum Chem.* **114**, 1287–1317.
Dovesi, R., Saunders, V. R., Roetti, C., Orlando, R., Zicovich-Wilson, C. M., Pascale, F., Civalleri, B., Doll, K., Harrison, N. M., Bush, I. J., D'Arco, P., Llunell, M., Causà, M. & Noël, Y. (2014). *CRYSTAL14 User's Manual.* University of Turin, Italy.
Ernst, M., Genoni, A. & Macchi, P. (2020). *J. Mol. Struct.* **1209**, 127975.
Field, M. J., Bash, P. A. & Karplus, M. (1990). *J. Comput. Chem.* **11**, 700–733.
Folkestad, S. D., Kjønstad, E. F., Goletto, L. & Koch, H. (2021). *J. Chem. Theory Comput.* **17**, 714–726.
Fornili, A., Sironi, M. & Raimondi, M. (2003). *J. Mol. Struct. Theochem*, **632**, 157–172.
Frisch, M. J., Trucks, G. W., Schlegel, H. B., Scuseria, G. E., Robb, M. A., Cheeseman, J. R., Scalmani, G., Barone, V., Mennucci, B., Petersson, G. A., Nakatsuji, H., Caricato, M., Li, X., Hratchian, H. P., Izmaylov, A. F., Bloino, J., Zheng, G., Sonnenberg, J. L., Hada, M., Ehara, M., Toyota, K., Fukuda, R., Hasegawa, J., Ishida, M., Nakajima, T., Honda, Y., Kitao, O., Nakai, H., Vreven, T., Montgomery, J. A. Jr, Peralta, J. E., Ogliaro, F., Bearpark, M., Heyd, J. J., Brothers, E., Kudin, K. N., Staroverov, V. N., Kobayashi, R., Normand, J., Raghavachari, K., Rendell, A., Burant, J. C., Iyengar, S. S., Tomasi, J., Cossi, M., Rega, N., Millam, J. M., Klene, M., Knox, J. E., Cross, J. B., Bakken, V., Adamo, C., Jaramillo, J., Gomperts, R., Stratmann, R. E., Yazyev, O., Austin, A. J., Cammi, R., Pomelli, C., Ochterski, J. W., Martin, R. L., Morokuma, K., Zakrzewski, V. G., Voth, G. A., Salvador, P., Dannenberg, J. J., Dapprich, S., Daniels, A. D., Farkas, Ö., Foresman, J. B., Ortiz, J. V., Cioslowski, J. & Fox, D. J. (2009). *Gaussian 09*, Revision D.01. Gaussian, Inc., Wallingford, CT, USA.

Fugel, M., Malaspina, L. A., Pal, R., Thomas, S. P., Shi, M. W., Spackman, M. A., Sugimoto, K. & Grabowsky, S. (2019). *Chem. Eur. J.* **25**, 6523–6532.
Gao, J. (1996). *Reviews in Computational Chemistry*, edited by K. B. Lipkowitz & D. B. Boyd, pp. 119–186. Weinheim, Germany: VCH Publishers.
Genoni, A. (2013*a*). *J. Phys. Chem. Lett.* **4**, 1093–1099.
Genoni, A. (2013*b*). *J. Chem. Theory Comput.* **9**, 3004–3019.
Genoni, A. (2017). *Acta Cryst.* A**73**, 312–316.
Genoni, A., Bučinský, L., Claiser, N., Contreras–García, J., Dittrich, B., Dominiak, P. M., Espinosa, E., Gatti, C., Giannozzi, P., Gillet, J.-M., Jayatilaka, D., Macchi, P., Madsen, A. Ø., Massa, L. J., Matta, C. F., Merz, K. M. Jr, Nakashima, P. N. H., Ott, H., Ryde, U., Schwarz, K., Sierka, M. & Grabowsky, S. (2018). *Chem. Eur. J.* **24**, 10881–10905.
Genoni, A., Dos Santos, L. H. R., Meyer, B. & Macchi, P. (2017). *IUCrJ*, **4**, 136–146.
Genoni, A., Franchini, D., Pieraccini, S. & Sironi, M. (2018). *Chem. Eur. J.* **24**, 15507–15511.
Genoni, A., Ghitti, M., Pieraccini, S. & Sironi, M. (2005). *Chem. Phys. Lett.* **415**, 256–260.
Genoni, A. & Macchi, P. (2020). *Crystals*, **10**, 473.
Genoni, A., Macetti, G., Franchini, D., Pieraccini, S. & Sironi, M. (2019). *Acta Cryst.* A**75**, 778–797.
Genoni, A., Merz, K. M. Jr & Sironi, M. (2008). *J. Chem. Phys.* **129**, 054101.
Genoni, A. & Meyer, B. (2016). *Adv. Quantum Chem.* **73**, 333–362.
Grabowsky, S., Genoni, A. & Bürgi, H.-B. (2017). *Chem. Sci.* **8**, 4159–4176.
Grabowsky, S., Genoni, A., Thomas, S. P. & Jayatilaka, D. (2020). *21st Century Challenges in Chemical Crystallography II – Structural Correlations and Data Interpretation*, *Structure and Bonding*, Vol. 186, edited by D. M. P. Mingos & P. Raithby, pp. 65–144. Cham: Springer Nature.
Grabowsky, S., Jayatilaka, S., Mebs, S. & Luger, P. (2010). *Chem. Eur. J.* **16**, 12818–12821.
Grabowsky, S., Luger, P., Buschmann, J., Schneider, T., Schirmeister, T., Sobolev, A. N. & Jayatilaka, D. (2012). *Angew. Chem. Int. Ed.* **51**, 6776–6779.
Grabowsky, S., Weber, M., Jayatilaka, D., Chen, Y.-S., Grabowski, M. T., Brehme, R., Hesse, M., Schirmeister, T. & Luger, P. (2011). *J. Phys. Chem. A*, **115**, 12715–12732.
Grimwood, D. J., Bytheway, I. & Jayatilaka, D. (2003). *J. Comput. Chem.* **24**, 470–483.
Grimwood, D. J. & Jayatilaka, D. (2001). *Acta Cryst.* A**57**, 87–100.
Guest, M. F., Bush, I. J., Van Dam, H. J. J., Sherwood, P., Thomas, J. M. H., Van Lenthe, J. H., Havenith, R. W. A. & Kendrick, J. (2005). *Mol. Phys.* **103**, 719–747.
Hickstein, D. D., Cole, J. M., Turner, M. J. & Jayatilaka, D. (2013). *J. Chem. Phys.* **139**, 064108.
Hudák, M., Jayatilaka, D., Perašínová, L., Biskupič, S., Kožíšek, J. & Bučinský, L. (2010). *Acta Cryst.* A**66**, 78–92.
Jayatilaka, D. (1998). *Phys. Rev. Lett.* **80**, 798–801.
Jayatilaka, D. (2012). *Modern Charge-Density Analysis*, edited by C. Gatti & P. Macchi, pp. 213–257. Dordrecht: Springer Netherlands.
Jayatilaka, D. & Dittrich, B. (2008). *Acta Cryst.* A**64**, 383–393.
Jayatilaka, D. & Grimwood, D. (2004). *Acta Cryst.* A**60**, 111–119.
Jayatilaka, D. & Grimwood, D. J. (2001). *Acta Cryst.* A**57**, 76–86.
Jayatilaka, D., Munshi, P., Turner, M. J., Howard, J. A. K. & Spackman, M. A. (2009). *Phys. Chem. Chem. Phys.* **11**, 7209–7218.
Kleemiss, F., Dolomanov, O. V., Bodensteiner, M., Peyerimhoff, N., Midgley, L., Bourhis, L. J., Genoni, A., Malaspina, L. A., Jayatilaka, D., Spencer, J. L., White, F., Grundkötter-Stock, B., Steinhauer, S., Lentz, D., Puschmann, H. & Grabowsky, S. (2021). *Chem. Sci.* **12**, 1675–1692.
Lee, S. J. R., Welborn, M., Manby, F. R. & Miller, T. F. III (2019). *Acc. Chem. Res.* **52**, 1359–1368.
Macchi, P. (2020). *Crystallogr. Rev.* **26**, 209–268.
Macetti, G. & Genoni, A. (2019). *J. Phys. Chem. A*, **123**, 9420–9428.
Macetti, G. & Genoni, A. (2020). *J. Chem. Theory Comput.* **16**, 7490–7506.
Macetti, G. & Genoni, A. (2021*a*). *Adv. Quantum Chem.* https://doi.org/10.1016/bs.aiq.2021.05.004.
Macetti, G. & Genoni, A. (2021*b*). *J. Chem. Theory Comput.* **17**, 4169–4182.
Macetti, G. & Genoni, A. (2021*c*). *J. Phys. Chem. A*, **125**, 6013–6027.
Macetti, G., Wieduwilt, E. K., Assfeld, X. & Genoni, A. (2020). *J. Chem. Theory Comput.* **16**, 3578–3596.
Macetti, G., Wieduwilt, E. K. & Genoni, A. (2021). *J. Phys. Chem. A*, **125**, 2709–2726.
Malaspina, L. A., Wieduwilt, E. K., Bergmann, J., Kleemiss, F., Meyer, B., Ruiz-López, M. F., Pal, R., Hupf, E., Beckmann, J., Piltz, R. O., Edwards, A. J., Grabowsky, S. & Genoni, A. (2019). *J. Phys. Chem. Lett.* **10**, 6973–6982.
Manby, F. R., Stella, M., Goodpaster, J. D. & Miller, T. F. III (2012). *J. Chem. Theory Comput.* **8**, 2564–2568.
Marrazzini, G., Giovannini, T., Scavino, M., Egidi, F., Cappelli, C. & Koch, H. (2021). *J. Chem. Theory Comput.* **17**, 791–803.
Massa, L. & Matta, C. F. (2018). *J. Comput. Chem.* **39**, 1021–1028.
Meyer, B. & Genoni, A. (2018). *J. Phys. Chem. A*, **122**, 8965–8981.
Meyer, B., Guillot, B., Ruiz-Lopez, M. F. & Genoni, A. (2016*a*). *J. Chem. Theory Comput.* **12**, 1052–1067.
Meyer, B., Guillot, B., Ruiz-Lopez, M. F., Jelsch, C. & Genoni, A. (2016*b*). *J. Chem. Theory Comput.* **12**, 1068–1081.
Philipp, D. M. & Friesner, R. A. (1999). *J. Comput. Chem.* **20**, 1468–1494.
Ricardi, N., Ernst, M., Macchi, P. & Wesolowski, T. A. (2020). *Acta Cryst.* A**76**, 571–579.
Saether, S., Kjaergaard, T., Koch, H. & Høyvik, I.-M. (2017). *J. Chem. Theory Comput.* **13**, 5282–5290.
Senn, H. M. & Thiel, W. (2009). *Angew. Chem. Int. Ed.* **48**, 1198–1229.
Sironi, M., Genoni, A., Civera, M., Pieraccini, S. & Ghitti, M. (2007). *Theor. Chem. Acc.* **117**, 685–698.
Sironi, M., Ghitti, M., Genoni, A., Saladino, G. & Pieraccini, S. (2009). *J. Mol. Struct. Theochem*, **898**, 8–16.
Stoll, H., Wagenblast, G. & Preuss, H. (1980). *Theor. Chim. Acta*, **57**, 169–178.
Sun, Q. & Chan, G. K.-L. (2016). *Acc. Chem. Res.* **49**, 2705–2712.
Thomas, S. P., Jayatilaka, D. & Guru Row, T. N. (2015). *Phys. Chem. Chem. Phys.* **17**, 25411–25420.
Warshel, A. & Levitt, M. (1976). *J. Mol. Biol.* **103**, 227–249.
Wesołowski, T. A. (2008). *Phys. Rev. A*, **77**, 012504.
Wesolowski, T. A., Shedge, S. & Zhou, X. (2015). *Chem. Rev.* **115**, 5891–5928.
Wesolowski, T. A. & Warshel, A. (1993). *J. Phys. Chem.* **97**, 8050–8053.
Whitten, A. E., Jayatilaka, D. & Spackman, M. (2006). *J. Chem. Phys.* **125**, 174505.
Wieduwilt, E. K., Macetti, G. & Genoni, A. (2021). *J. Phys. Chem. Lett.* **12**, 463–471.
Wieduwilt, E. K., Macetti, G., Scatena, R., Macchi, P. & Genoni, A. (2021). *Crystals*, **11**, 207.
Zhou, Q.-L., Zhang, Z.-H. & Jing, Z. L. (2007). *Acta Cryst.* E**63**, o3039.